Journal of Molecular Structure (Theochem), 307 (1994) 201–215
0166-1280/94/$07.00

Is $(NH_3)_2$ hydrogen bonded?

E.H.T. Olthof, A. van der Avoird*, P.E.S. Wormer

Institute of Theoretical Chemistry, University of Nijmegen, Toernooiveld, 6525 ED Nijmegen, Netherlands

(Received 20 October 1993; accepted 25 October 1993)

Abstract

Vibration–rotation–tunneling (VRT) splittings have been computed for the dimer $(NH_3)_2$ by the use of four different model potentials. The six-dimensional nuclear motion problem is solved variationally in a symmetry adapted basis consisting of analytic radial functions and rigid rotor functions depending on the five internal angles, as well as on the three overall rotation angles. Two of the potentials are designed such that they have no barrier for interchange tunneling and the other two potentials have barriers of 31.1 and 24.4 cm^{-1}, respectively. The top of the barrier corresponds to a cyclic structure and the two equivalent minima on either side of the barrier to nearly linear hydrogen bonds.

Energy splittings, dipole moments, nuclear quadrupole splittings, and the amount of quenching of the monomer umbrella inversions are computed and compared with the available experimental numbers. The potential that gives best agreement with the observed quantities has an equilibrium hydrogen bonded structure close to linear, but a VRT-averaged ground state structure that is nearly cyclic.

1. Introduction

It is a fact, well-established theoretically [1–10] and experimentally [11–16], that the dimers $(HF)_2$ and $(H_2O)_2$ have a hydrogen bonded structure. Until 1985 it was generally believed that the ammonia dimer, too, had a "classical" hydrogen bonded structure with a proton of one monomer pointing to the nitrogen lone pair of the other. In that year Nelson et al. [17] interpreted their microwave spectra by assuming that the dimer has a nearly cyclic structure in which the two umbrellas are almost anti-parallel. This interpretation was not supported by most of the ab initio calculations in existence at the time, and spurred theoreticians to undertake more elaborate calculations [18–21], most of which still yield a hydrogen bonded equilibrium structure. The two most recent — and most sophisticated — calculations differ in the prediction of the equilibrium structure: Hasset et al. [22] found a hydrogen bonded structure, whereas Tao and Klemperer [23] found a cyclic structure thanks to the addition of bond functions.

An obvious explanation of the discrepancy between the outcome of most calculations and the microwave data may be found in the effect of vibrational averaging: whereas the electronic structure calculations focus mainly on finding the minimum of the intermolecular potential, the experiment gives a vibrationally averaged structure. The potential energy surface being flat in several directions [22,23], it is very hard, however, to compute the vibrationally averaged geometry and to explain the discrepancy quantitatively. On the one hand the flatness of the surface indicates that the difference between equilibrium and vibrationally averaged structure can indeed be substantial, but on the other hand it also means that a simple harmonic model does not suffice. A full six-dimensional solution of the nuclear Schrödinger equation is required to make a definite assessment of the expectation values of the relevant nuclear

* Corresponding author.

SSDI 0166-1280(94)03662-5

coordinates. Such a computation, in turn, requires a full six-dimensional potential energy surface, which is not available from ab initio calculations. Most ab initio work gives only selected cuts through the surface. This allows only the fitting of a crude model potential that subsequently can be used to extrapolate to regions of the surface not covered by the electronic structure calculations. In this manner Sagarik et al. [18] obtained earlier a potential for the ammonia dimer from coupled pair functional calculations. We used this potential in a series of extensive calculations [24] in which we solved the full six-dimensional nuclear motion equation.

Although we found that the vibrationally averaged structure was shifted from the equilibrium hydrogen bonded structure toward the cyclic geometry, we were not able to obtain complete reconciliation with the microwave geometry. Since our potential was not very reliable, our results were not conclusive, although they did show that the dimer is floppy and that accordingly the effect of vibrational averaging is very important, not only for the geometry, but also for other measured properties such as the dipole moment and nuclear quadrupole splittings. Further we obtained indirect evidence that the "umbrella" inversion of the two monomers is not completely quenched, as was assumed by Nelson et al. [17].

The latter conclusion was also reached by Loeser et al. [25], who reported an extensive set of new far-infrared and microwave measurements and gave a very detailed analysis of these — as well as previous [26] — experimental data. They conclude that the group of feasible operations (permutations, inversion and their products) is of order 144, which means that they observed the tunneling splittings associated with the two umbrella inversions and the interchange tunneling in which the role of the two monomers is reversed. In this connection we also want to mention the work of the Nijmegen/Bonn group [27], who reported tunneling splittings in the far-infrared, including those due to umbrella tunneling. Recently they also measured the dipole moment in the $|\Omega| = 1$ state of G-symmetry [28]. We predicted earlier [24] that the dipole moments of the $|\Omega| \geqslant 1$ states of E_3 and E_4 symmetry are also non-vanishing; it will be interesting if this prediction can be verified experimentally.

In this paper we will study the influence of the intermolecular potential on the computed vibration–rotation–tunneling (VRT) states. We will investigate which different vibrationally averaged structures are obtained from different model potentials and how other observed properties are affected by these potentials.

2. Model potentials

We have investigated four different model potentials that all depart from a simple electrostatic model in which each monomer is described as a point dipole and quadrupole, located at the monomer center of nuclear mass. See Table 1 for the structure of ammonia, taken from the work of Dykstra and Andrews [29], and Table 2 for the values of the electrostatic moments [30]. Fixing the distance between the mass centers at $R = 3.23$ Å, we find a minimum in the potential for $\theta_A = 18°$ and $180° - \theta_B = 100°$, where the angles are defined in Fig. 1. These are the angles expected in a hydrogen bonded structure. Note, however, that the energy in this simple model does not depend on ϕ_A or ϕ_B, because the dipole and the quadrupole tensor are axial, both having only a non-vanishing component along the three-fold symmetry axis of the monomer. This freedom implies that the positions of the protons of monomer B are undetermined with respect to the lone pair of monomer A.

Next we added a point octupole to both molecules, which has the effect that monomer B rotates around its three-fold axis such that one of its protons is close to the lone pair of A. The minimum structure is at $(\theta_A, 180° - \theta_B) = (20°, 99)$ and $(\phi_A, \phi_B) = (60°, 0°)$($R$ still fixed at 3.23 Å). Thus, this simple electrostatic model predicts already the classical hydrogen-bonded structure with its

Table 1
Ammonia structure[a]

Bond	Length (Å)
r_{HC}	0.988 51
r_{HN}	1.012 00
r_{NC}	0.067 66
r_{LN}	0.988 51

[a] C is the center of mass, L is lone pair force center.

characteristic well-directed bond. We conclude that the hydrogen bond has a purely electrostatic origin, no resonances between covalent and ionic structures [31] are needed to obtain a directed bond.

When we vary simultaneously $(\theta_A, 180° - \theta_B)$ from the one minimum at (20°, 99°) to the other equivalent minimum at (81°, 160°), while minimizing the energy by relaxing the angles γ, ϕ_A, and ϕ_B, we walk over the interchange tunnelling path. The barrier that is herewith crossed has height $126.8\,cm^{-1}$ on the dipole–quadrupole–octupole surface, see Fig. 2, where we exhibit the energy as a function of θ_A and θ_B. Note that electrostatics allows interchange tunneling only through a narrow valley.

Next we introduce the exchange repulsion and dispersion attraction in the form of an exp-6 site–site potential,

$$V_{AB} = \sum_{i\in A}\sum_{j\in B}\left[A_i A_j \exp[-(b_i + b_j)R_{ij}] - \frac{c_i c_j}{R_{ij}^6}\right] \quad (1)$$

Following the work of Dykstra and Andrews [29], we considered in addition to the nitrogen nuclei and protons also the nitrogen lone pairs as centers of force. See Table 1 for the locations of these centers and Table 2 for different sets of force field parameters used in this work. The parameters c_i were simply taken from Dykstra et al. The parameters A_i and b_i in potential I were determined from the (6–12) Lennard-Jones (LJ) potential of Dykstra et al. by requiring that the depth and the position of the minimum in the N–N and H–H terms of Eq. (1) coincide with the minimum in the corresponding term of the LJ potential. The reason why we did not use the LJ potential itself was the following. Our dynamics program requires the potential as a linear combination of angular functions, see below, so that we always expand our model potentials. We experienced convergence problems when we tried to expand the (6–12) LJ potential. Switching to the exp-6 potential solved this problem.

Since the Dykstra potential does not contain

Table 2
Potentials [a.u.][a]

Parameter[a]	I	II	III	IV
Q_0^1	−0.6106	−0.6106	−0.6106	−0.6106
Q_0^2	−2.1598	−2.1598	−2.1598	−2.1598
Q_0^3	0.0	0.0	2.5226	2.5226
Q_3^3	0.0	0.0	4.1748	4.1748
c_N	14.0	14.0	14.0	14.0
c_L	0.0	0.0	0.0	0.0
c_H	0.2	0.2	0.2	0.2
b_N	1.8391	1.8391	1.8391	1.8391
b_L	1.5549	1.5549	1.5549	1.5549
b_H	1.5549	1.5549	1.5549	1.5549
A_N	207.	207.	280.	255.
A_L	9.336(−4)	8.000(−3)	5.000(−4)	2.000(−3)
A_H	1.541(−2)	4.880(−2)	1.000(−2)	1.540(−2)

[a] Electric moments from Ref. 30, for the other parameters see text. Numbers in parentheses indicate powers of ten.

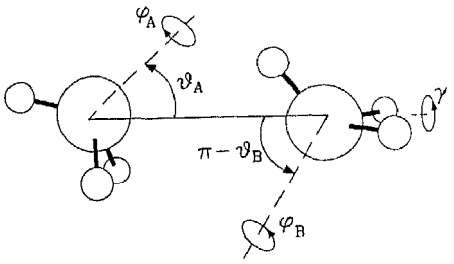

Fig. 1. The relevant coordinates of the dimer. The angles are defined as follows: We take two parallel frames centered on A and B and let the positive z-axes point from the center of mass of A to that of B. The plane of the drawing coincides with the xz-planes with the x-axes pointing upward. Consider a geometry with two parallel umbrellas, the symmetry axes on the z-axes and the plane of paper as a symmetry plane. Each monomer has an NH bond in its xz-plane with positive x-coordinate and negative z. This is the geometry with all angles zero. Next we rotate the symmetry axes such that they have polar angles $\theta_X, \gamma X$, where X = A or B. Then $\gamma = \gamma_B - \gamma_A$. Finally we rotate the monomers around their symmetry axes over angles ϕ_A and ϕ_B, respectively. A positive rotation is in the direction of the lone pair.

octupoles, we obtain too much attraction when adding octupoles (potential **III** and **IV**), which we compensated by increasing the parameter A_N somewhat. Since the nitrogen atoms almost coincide with the respective centers of mass, this hardly affects the anisotropy in the interaction.

Potential **I**, which by design resembles the Dykstra potential, has an interchange barrier of 31.1 cm^{-1}. By increasing A_L and A_H we obtained potential **II**. Since an increase of these parameters lowers the barrier, we could achieve that a minimum occurs in potential **II** at about the position of the saddle point of **I**. Thus potential **II** was designed to have its minimum for a cyclic structure. Notice parenthetically that we present values of $180° - \theta_B$ in Table 3, rather than of θ_B, because whenever $\theta_A \approx 180° - \theta_B$, we have a cyclic structure. Potential **III** is the counterpart of **I** with an octupole added and **IV** resembles potential **II** in its interchange behavior, but differs by the presence of an octupole. See Fig. 3 for an intersection of potential **III**; it is seen that the interchange

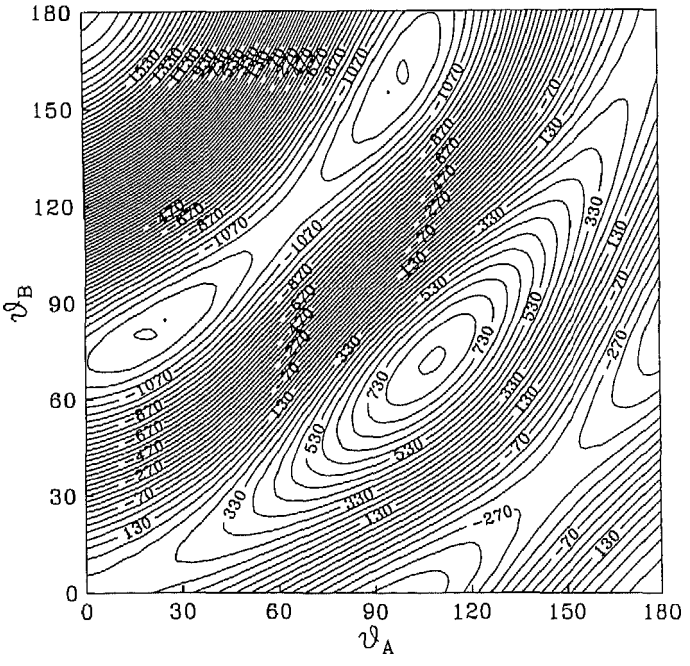

Fig. 2. The electrostatic dipole–quadrupole–octupole energy (cm^{-1}) as a function of θ_A and θ_B, ϕ_A and ϕ_B fixed at their equilibrium values (60°, 0°), $\gamma = 180°$ and $R = 3.23$ Å. Observe that the narrow valley for interchange tunneling is due to electrostatics. This valley persists when we add exchange and dispersion interactions.

Table 3
Equilibrium values and barrier heights in different potentials

Parameter[a]	I	II	III	IV[b]
R (Å)	3.236	3.296	3.366	3.330
θ_A (deg)	29.8	62.6	32.0	49.5
$180° - \theta_B$ (deg)	92.0	62.6	91.5	76.3
ϕ_A (deg)	0.0	0.0	60.0	60.0
ϕ_B (deg)	60.0	60.0	0.0	0.0
ΔE_{AB} (cm^{-1})	31.1	0.0	24.4	1.0
ΔE_A (cm^{-1})	2.16	32.71	26.7	80.86
ΔE_B (cm^{-1})	159.56	32.71	335.4	258.48

[a] ΔE_{AB} is the height of the saddle point in the θ_A, θ_B-plane (other coordinates relaxed). ΔE_X is the barrier crossed in varying ϕ_X, X = A or B (other coordinates at their equilibrium values).
[b] Although the equilibrium geometry in potential **IV** does not correspond to a cyclic structure, this potential is flat along the interchange tunneling path and its shape is almost equal to that of **II**, see Fig. 4.

tunneling path still runs through the valley caused by the electrostatic part of the potential (cf. Fig. 2). The ϕ_A and ϕ_B dependence of **I** vs. **III** and **II** vs. **IV** are completely different, of course, because of the octupoles.

The addition of the exp-6 terms to the electrostatic potential influences the equilibrium structure. Due to the repulsive terms the proton of B in the hydrogen bond tries to avoid the lone pair of A, so that both molecules are rotated towards a cyclic minimum by a simultaneous increase of θ_A and θ_B. In potential **I** the effect is modest, but in **II**, with its much more active lone pair, the equilibrium structure is cyclic.

The site–site intermolecular potentials are

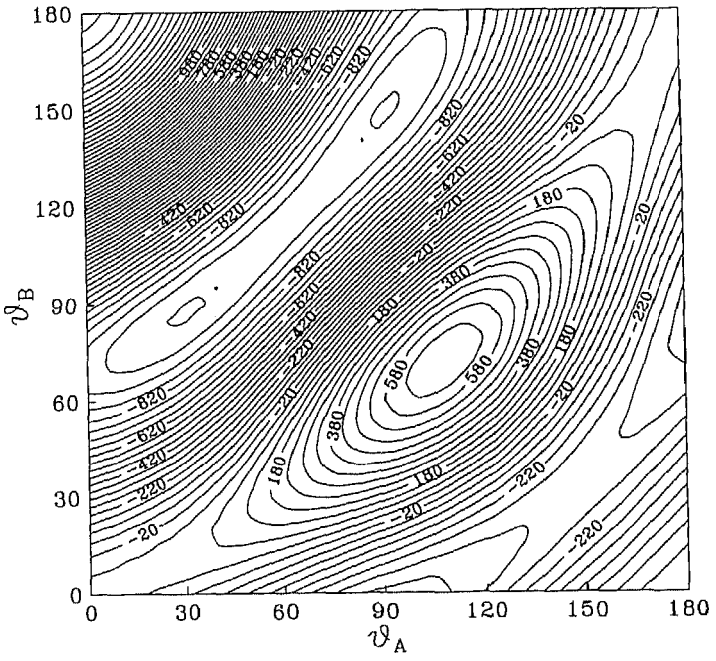

Fig. 3. Potential **III** (cm^{-1}) as a function of θ_A and θ_B, ϕ_A and ϕ_B fixed at their equilibrium values (60°, 0°). Observe the same valley for interchange tunneling as in the purely electrostatic case of Fig. 2.

expanded in a complete set of angular functions

$$V_{\text{int}}(R, \gamma_A, \theta_A, \varphi_A, \gamma_B, \theta_B, \varphi_B) = \sum_{\Lambda} \nu_{\Lambda}(R) \times A_{\Lambda}(\gamma_A, \theta_A, \varphi_A, \gamma_B, \theta_B, \varphi_B) \quad (2)$$

We do this because our dynamics program calculates the angular parts of the matrix elements analytically by the techniques of angular momentum theory. The electrostatic, multipole expanded, potential can be written analytically in terms of these angular functions, with the coefficient $\nu_{\Lambda}(R)$ being proportional to $R^{-L_A-L_B-1}$ times the product of the monomer multipole moments $Q_{K_A}^{L_A}$ and $Q_{K_B}^{L_B}$. The angular functions are rotational invariants defined by

$$A_{\Lambda}(\gamma_A, \theta_A, \varphi_A, \gamma_B, \theta_B, \varphi_B) = \sum_{M} \begin{pmatrix} L_A & L_B & L \\ M & -M & 0 \end{pmatrix} \times D_{MK_A}^{(L_A)*}(\gamma_A, \theta_A, \varphi_A) D_{-MK_B}^{(L_B)*}(\gamma_B, \theta_B, \varphi_B) \quad (3)$$

Here Λ stands for the set of quantum numbers (L_A, K_A, L_B, K_B, L), D denotes a Wigner rotation function and the quantity in large brackets is the Wigner $3j$ symbol [32]. The potential depends only on internal angles, see Fig. 1, and — due to the definition of the $\boldsymbol{D}$-matrices — only on the difference angle $\gamma = \gamma_A - \gamma_B$. Because the time for the computation of the VRT states scales quadratically with $L_A^{\max}$ and $L_B^{\max}$, expansions to high order in L are very time consuming and therefore the expansions are usually truncated at $L_A^{\max} = L^{\max_B} = 5$.

One of the most important characteristics of the potentials being the interchange barrier, we tested in one case whether the barrier height changes under an increase of $L^{\max}$. We took the site–site potential of Sagarik et al. [18] and found that $L_A^{\max} = L_B^{\max} = 5$ gave virtually the same barrier ($73.5\,\text{cm}^{-1}$) as $L_A^{\max} = L_B^{\max} = 6$, which again was not far from the barrier ($83.5\,\text{cm}^{-1}$) in the original site–site potential. (This is in contrast to what we stated in our earlier paper [24], where the grid on which we relaxed the coordinates was taken too coarse, a finer grid gave a good agreement in barrier heights.)

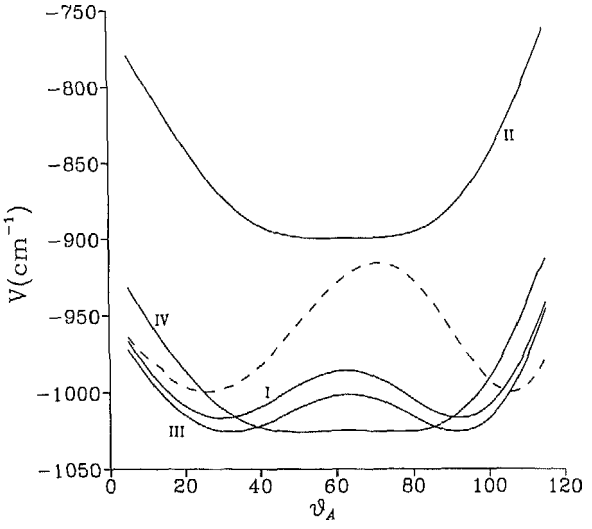

Fig. 4. The energy on the interchange path for four different model potentials, (cf. Table 3), indicated by full lines. The dashed line is the potential of Sagarik et al. [18]. Varied are θ_A and θ_B, the other coordinates are relaxed, so as to minimize the interaction energy.

In Fig. 4 the energy on the interchange path for four different potentials is shown together with the potential of Sagarik et al. [18] that we used in our earlier VRT calculations. Note that this potential has the highest barrier ($83.5\,\text{cm}^{-1}$), whereas potential **I** has only a barrier of $31.1\,\text{cm}^{-1}$ which is in close agreement with the ab initio barrier of Hassett et al. [22] ($29.3\,\text{cm}^{-1}$). Potential **III** has the even lower barrier of height of $24.4\,\text{cm}^{-1}$. Hassett et al. found their minimum at $(\phi_A, \phi_B) = (60°, 0°)$. Note from Table 3 that our potentials without octupoles yield minima for $(\phi_A, \phi_B) = (0°, 60°)$, and that potential **III** and **IV** agree with Hassett et al. in the minimum ϕ values. The recent potential by Tao and Klemperer [23] resembles in its θ-dependence potentials **II** and **IV**, which favor a cyclic structure.

3. Vibration–rotation–tunneling states

If we use the coordinate system defined in Fig. 1,

the Van der Waals Hamiltonian describing the motions in the ammonia dimer is [24,33]

$$\hat{H}_{\mathrm{vdw}} = \sum_{\lambda} A_{\lambda}[\hat{j}_{\mathrm{A}\lambda}^2 + \hat{j}_{\mathrm{B}\lambda}^2] + \frac{1}{2\mu R^2}[\hat{J}^2 + \hat{j}^2 - 2\hat{\boldsymbol{j}}\cdot\hat{\boldsymbol{J}}] - \frac{\hbar^2}{2\mu R}\frac{\partial^2}{\partial R^2}R + V_{\mathrm{int}}(\gamma_{\mathrm{A}}, \theta_{\mathrm{A}}, \varphi_{\mathrm{A}}, \gamma_{\mathrm{B}}, \theta_{\mathrm{B}}, \varphi_{\mathrm{B}}). \tag{4}$$

The first term in this Hamiltonian contains both rigid rotor Hamiltonians of the monomers, where $\hat{\boldsymbol{j}}_{\mathrm{A}}$ and $\hat{\boldsymbol{j}}_{\mathrm{B}}$ are the usual body-fixed angular momenta, and $\hat{\boldsymbol{j}} = \hat{\boldsymbol{j}}_{\mathrm{A}} + \hat{\boldsymbol{j}}_{\mathrm{B}}$. The rotational constants are taken as $A_x = A_y = 9.945\,\mathrm{cm}^{-1}$ and $A_z = 6.229\,\mathrm{cm}^{-1}$, which are the mean values of the rotational constants for the 0^+ and 0^- umbrella states given in Ref. 24. The second term describes the overall rotation of the dimer and the Coriolis interaction. The operator $\hat{\boldsymbol{j}}$ appearing in this term is the space-fixed variant of $\hat{\boldsymbol{j}}_{\mathrm{A}} + \hat{\boldsymbol{j}}_{\mathrm{B}}$ and the total angular momentum $\hat{\boldsymbol{J}}$ is a pseudo-angular momentum operator [33]. In the present work we have neglected the small off-diagonal Coriolis contribution contained in the term $\hat{\boldsymbol{j}}\cdot\hat{\boldsymbol{J}}/\mu R^2$. This implies that Ω, the component of $\boldsymbol{j}$ as well as $\boldsymbol{J}$ on the dimer z-axis, becomes a good quantum number. The third term is the kinetic energy belonging to the radial coordinate R, with μ denoting the reduced mass of the complex. With the values [34] $m_{\mathrm{H}} = 1.0078$ amu and $m_{\mathrm{N}} = 14.0031$ amu for the masses of hydrogen and $^{14}\mathrm{N}$, respectively, we get $\mu = 8.5133$ amu. The last term is the intermolecular potential introduced in Section 2.

In order to find a convenient basis for the diagonalization of $\hat{H}_{\mathrm{vdw}}$, we first diagonalized the Hamiltonian $\hat{H}_{\mathrm{rad}}$ defined by

$$\hat{H}_{\mathrm{rad}} = -\frac{\hbar^2}{2\mu R}\frac{\partial^2}{\partial R^2}R + V_{\mathrm{rad}}(R). \tag{5}$$

The radial potential $V_{\mathrm{rad}}(R)$ is found by fixing all angles to the values at the minimum of the expanded potential and varying R. The radial Hamiltonian $\hat{H}_{\mathrm{rad}}$ is diagonalized by taking a Morse-type basis, see Ref. 35 for more details. We calculate the bound states by diagonalizing $\hat{H}_{\mathrm{vdw}}$ in a symmetry adapted basis obtained from the following functions [24]

$$\begin{aligned}|j_{\mathrm{A}}, k_{\mathrm{A}}, j_{\mathrm{B}}, k_{\mathrm{B}}, j, \Omega, J, M, n\rangle &= \left[\frac{(2j_{\mathrm{A}}+1)(2j_{\mathrm{B}}+1)(2J+1)}{256\pi^5}\right]^{1/2} \\ &\times \sum_{\Omega_{\mathrm{A}},\Omega_{\mathrm{B}}} D^{(j_{\mathrm{A}})^*}_{\Omega_{\mathrm{A}}k_{\mathrm{A}}}(\gamma_{\mathrm{A}}, \theta_{\mathrm{A}}, \varphi_{\mathrm{A}}) D^{(j_{\mathrm{B}})^*}_{\Omega_{\mathrm{B}}k_{\mathrm{B}}}(\gamma_{\mathrm{B}}, \theta_{\mathrm{B}}, \varphi_{\mathrm{B}}) \\ &\times \langle j_{\mathrm{A}}\Omega_{\mathrm{A}} j_{\mathrm{B}}\Omega_{\mathrm{B}}|j\Omega\rangle D^{(J)^*}_{M\Omega}(\alpha, \beta, 0)\phi_n(R).\end{aligned} \tag{6}$$

The quantity in pointed brackets is an SO(3)-Clebsch–Gordan coefficient [32]. The radial functions $\phi_n(R)(n = 1,2,3)$ are the lowest three eigenfunctions of the radial Hamiltonian in Eq. (5). In most cases j_{A} and j_{B} were restricted to $j_{\max} = 5$, because of limited computer resources. Although the energy levels are not fully converged at $j_{\max} = 5$, the energy differences have converged much better and we expect the ordering of the levels to be correct for the intermolecular potential used.

The molecular symmetry group, which by definition consists of feasible permutations and inversion, is of order 36, provided we assume the umbrella inversions to be frozen. Otherwise it is of order 144. These groups are denoted G_{36} and G_{144}, respectively. In this work we will mainly focus on G_{36}, which has four one-dimensional irreducible representations (irreps), designated A_i, $i = 1, \ldots, 4$, four two-dimensional irreps (E_i, $i = 1, \ldots, 4$) and one four-dimensional irrep G. The kets of A_i symmetry are states of two ortho monomers, those of E_i symmetry belong to two para monomers and G kets describe a mixed ortho–para dimer. For more details on the symmetry adaption of our basis we refer to the Appendix of Ref. 24.

The group G_{36} contains two interchange generators, referred to in Ref. 24 by $\hat{I}_1$ and $\hat{I}_2$. States of A_1 symmetry are symmetric and states of A_4 are antisymmetric under the action of $\hat{I}_1$ and $\hat{I}_2$. Thus, the splitting between the energies of the lowest A_1 and A_4 states is due to interchange tunneling and is indicative for the barrier height and width in the interchange tunneling path. Because of this direct

dependence of the A_1/A_4 energies on the interchange, and to gain some insight in the convergence with respect to basis size, we have computed these energies with different expansion lengths of the basis. Using potential I, we truncated at $j_{max} = 5, 6$ and 7. The respective A_1 energies are: -660, -665, and $-667\,cm^{-1}$, and the A_4 energies: -640, -649, and $-652\,cm^{-1}$. So we see that, although the energies themselves are not converged yet, their splittings (20, 16 and $15\,cm^{-1}$, respectively) are closer to the basis set limit. Considering the crudeness of the potentials and the costs of the dynamic calculations, we decided to perform all the calculations with $j_{max} = 5$.

In Fig. 5 the lowest wavefunction of A_1 symmetry is presented as a function of θ_A and θ_B, the other coordinates fixed at their equilibrium values. In Fig. 6 we find the lowest wavefunction of A_4 symmetry. Evidently, the symmetry is of importance for the character of the wavefunction. Whereas the A_1 state is symmetric, the A_4 state is antisymmetric under $\theta_A \leftrightarrow 180° - \theta_B$.

Figure 7 exhibits a cut through the absolute square of the lowest wavefunction of G symmetry. This function was obtained from the diagonalization of H_{vdw} containing potential **III** defined in Table 3. Note the localization on the one side of the interchange barrier, which can be understood from the inequivalence of ortho and para monomers. First recall [24] that the G-states are symmetrized products of ortho (proton spins coupled to a quartet) and para (proton spins coupled to a doublet) ammonia wavefunctions. Monomer A is ortho and monomer B is para. Recall also that the free ortho ammonia rigid rotor wavefunctions have a quantum number $k \equiv 0 \pmod 3$ and that para monomers have $k \equiv \pm 1 \pmod 3$, where k is the projection of the monomer angular momentum on the three-fold symmetry axis. Since one must mix states starting with a total angular quantum number equal to 3, it takes more energy to localize in ϕ an ortho ammonia than a para ammonia. In the complex this means that a structure is more favorable in which the rotation around ϕ of the ortho ammonia is less hindered than the rotation of the para ammonia. In the structure with $\theta_A = 30°$ and $\theta_B = 90°$ and potential I the rotation of monomer A is hardly

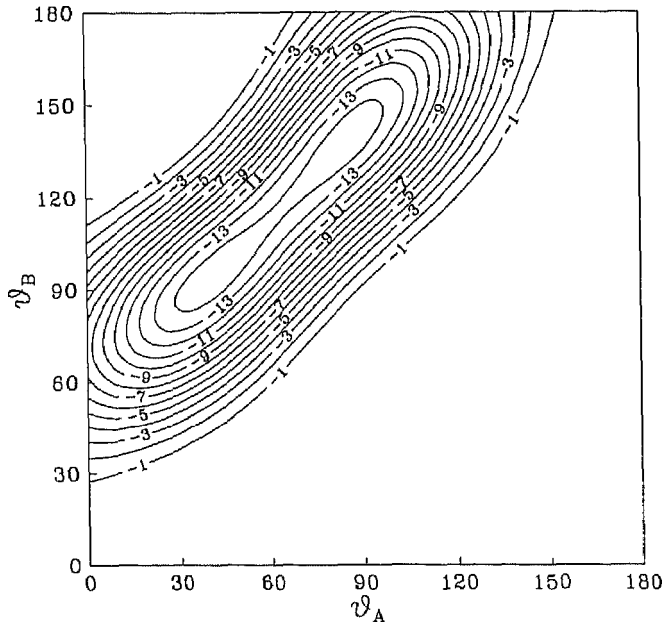

Fig. 5. The lowest wavefunction of A_1 symmetry, symmetric under $\theta_A \leftrightarrow 180° - \theta_B$, obtained from potential **III**.

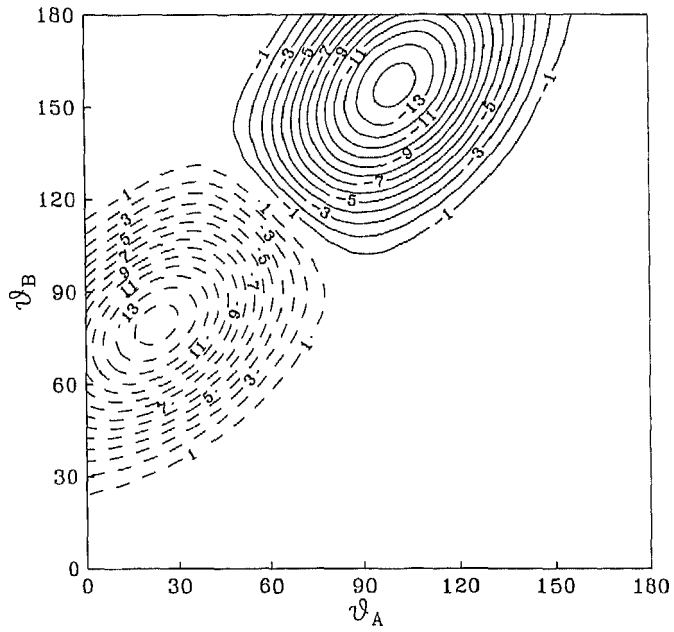

Fig. 6. The lowest wavefunction of A_4 symmetry, antisymmetric under $\theta_A \leftrightarrow 180^\circ - \theta_B$, obtained from potential III.

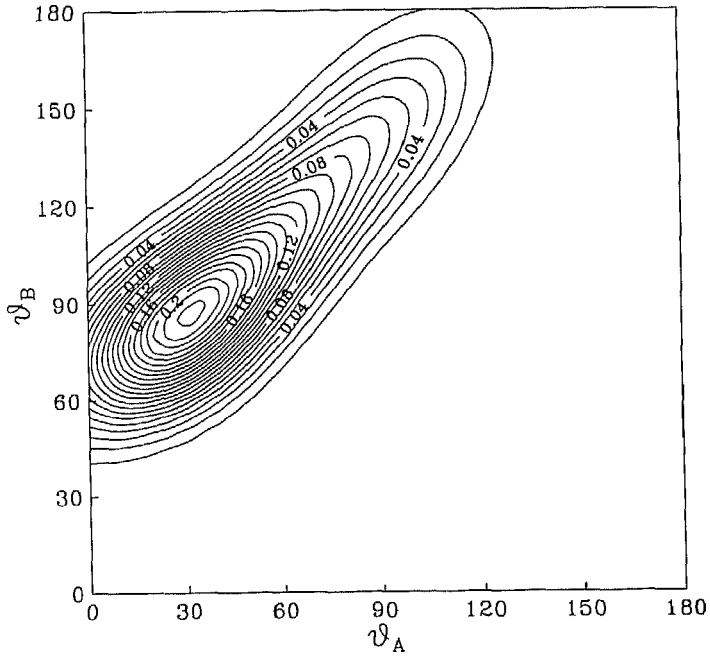

Fig. 7. The lowest wavefunction (absolute squared) of G symmetry in the $\theta_A - \theta_B$ plane obtained from potential III.

hindered, whereas a rotation of B around ϕ is hindered due to the repulsion of its protons with the lone pair of A. Remember that in potentials **III** and **IV** also the octupoles add to the barriers in the rotations over ϕ_A and ϕ_B.

In Fig. 8 we see the probability amplitude of the lowest state of G symmetry obtained from potential **IV**. This potential was constructed such that it has practically no barrier at the cyclic structure $\theta_A = 180° - \theta_B$ and yet the amplitude has a maximum shifted somewhat toward the hydrogen-bonded structure. Again, this must be ascribed to the non-equivalence of the rotation in ϕ of the ortho and para monomer constituting the dimer in a G state.

The difference between the lowest energy (E_G) and the one but lowest (E'_G) of G symmetry is partly due to the ortho-para splitting and partly to the interchange tunneling. To some extent this splitting is therefore also indicative for the height of the interchange barrier, see Table 4. The energy splitting between states of E_1 and E_2 symmetry, too, is mainly due to interchange tunneling; it is 535, 825, 603, and 886 GHz for potentials ***I*** through to **IV**, respectively, see Table 4. This may be compared with the experimental number [25] 577 GHz. However, the states of E_1 and E_3 symmetry have more or less the same character with respect to interchange tunneling, but differ in their k quantum numbers and hence in their dependence on ϕ_A and ϕ_B. Their computed splitting is an order of magnitude smaller than the E_1/E_2 splitting, but still about three orders of magnitude too large in comparison with experiment, see the row in Table 4 labelled by $E_{E_1} - E_{E_3}$. The same remarks apply to the $E_{E_2} - E_{E_4}$ splitting, where we compute 145.7 GHz (in potential **III**), whereas the experimental value is a hundred times smaller (1.50 GHz) [25].

The final two splittings in Table 4 are owing to monomer umbrella inversion. An exact calculation requires the solution of an eight-dimensional dynamics problem: the six coordinates of Fig. 1 plus the two umbrella angles ρ_A and ρ_B. The group of this system is G_{144} and the labels $G_2^{\pm}$ refer to irreps of this group. These irreps correlate

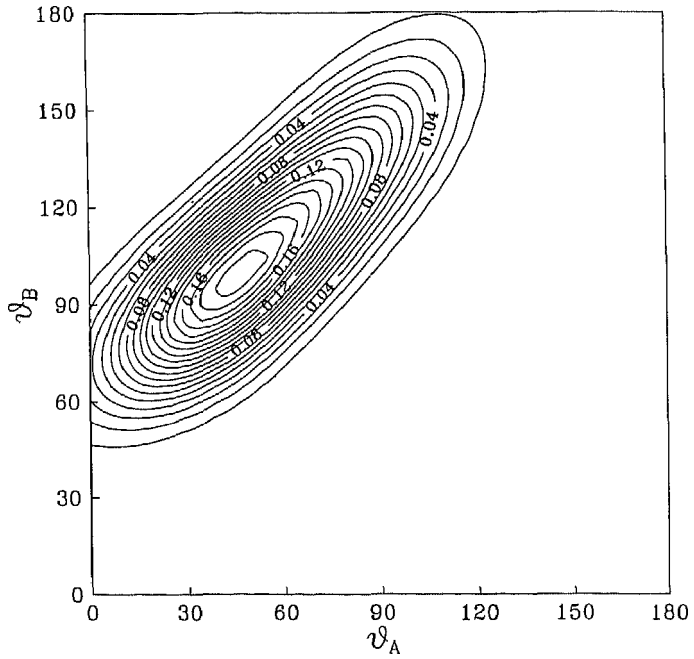

Fig. 8. The lowest wavefunction (absolute squared) of G symmetry in the $\theta_A - \theta_B$ plane obtained from potential **IV**.

Table 4
Comparison of computed and measured quantities. All quantities pertain to $\Omega = 0$

	I	II	III	IV	Exp.
$\langle\theta_A\rangle_G$ [a] (deg)	54	60	51	59	–
$\langle 180^\circ - \theta_B\rangle_G$ [a] (deg)	81	73	86	79	–
Dipole[b] (D)	−0.69	−0.32	−0.92	−0.53	0.74
$\langle\theta_A\rangle_G$ [c] (deg)	46	53	44	51	49
$\langle 180^\circ - \theta_B\rangle_G$ [c] (deg)	63	62	66	64	65
$E'_G - E_G$ (GHz)[d]	637	965	680	879	614
$E_{A_4} - E_{A_1}$ (GHz)[d]	587	1027	509	779	483
$E_{E_1} - E_{E_2}$ (GHz)[d]	535	825	603	886	577
$E_{E_1} - E_{E_3}$ (GHz)[d]	43.5	53.7	69.7	46.3	0.167
$E_{E_2} - E_{E_4}$ (GHz)[d]	40.0	114.1	145.7	150.9	1.50
$E_{G_2^-} - E_{G_2^+}$ (GHz)[d]	2.49	1.19	3.12	1.89	3.31
$E'_{G_2^-} - E'_{G_2^+}$ (GHz)[d]	1.40	0.82	1.21	1.76	2.39

[a] From $\langle P_1(\cos\theta)\rangle$; G ground state.
[b] G ground state. Experimentally the sign is undetermined.
[c] From $\langle P_2(\cos\theta)\rangle$; G ground state.
[d] 1 GHz = 0.03336 cm^{-1}.

with the irrep G of $G_{36} \subset G_{144}$. A dynamics problem of this size cannot be handled at present, so that we had to resort to a simple model which is an extension of a model we proposed earlier for Ar–NH_3 [36]. Briefly, the model entails the computation of the expectation value of the inversion parts of the monomer Hamiltonians, $H_{inv}(\rho_A) + H_{inv}(\rho_B)$, with respect to the functions $[E - (56)][E \mp (56)^*]\Psi_{vdw} f(\rho_A) f(\rho_B)$, where $(56)^*$ is the operator inverting monomer A and (56) inverts B. The wavefunction Ψ_{vdw} is the lowest, or the one but lowest, eigenstate of H_{vdw} of G symmetry, $f(\rho_A)$ and $f(\rho_B)$ are ground umbrella (ν_2) states of A and B localized in one of the wells of their respective monomers. Assuming that $\langle f(\rho_A)|(56)^*|f(\rho_A)\rangle = 0$ and an equivalent relation on B, we obtain for the splitting

$$E_{G_2^-} - E_{G_2^+} = \Delta\langle\Psi_{vdw}|(56)^*|\Psi_{vdw}\rangle$$

where $\Delta = 0.793\,\text{cm}^{-1}$, the tunneling splitting of the free monomer [37]. This splitting corresponds to the inversion of the para partner in the dimer. In a forthcoming paper [38] we will present more details on this model and its group theoretical implications.

In two ways we obtained vibrationally averaged angles: first by computation of the expectation values of the Legendre polynomial $P_1(\cos\theta_X)$, X = A or B and secondly by the expectation value of $P_2(\cos\theta_X)$. It is of interest to note that $\langle P_2(\cos\theta_A)\rangle$ and $\langle P_2(\cos\theta_B)\rangle$ follow separately from measurement of the ^{14}N quadrupole splitting in a G state. One splitting belongs to the ortho and the other to the para monomer. The measured dimer dipole moment, however, gives only information about the sum $\langle P_1(\cos\theta_A) + P_1(\cos\theta_B)\rangle$. In Table 4 we see that the angles obtained from $\langle P_1\rangle$ and $\langle P_2\rangle$ differ considerably, indicating that the dimer is indeed floppy in the angles θ_X. Further we see that all model potentials give fairly good agreement with the observed quadrupole splittings. The dipole overshoots somewhat when we add an octupole to potential **I**: we go from 0.69 to 0.92 D with the experimental number being 0.74 D.

Very recently the absolute value of the dipole moment of the lowest $|\Omega| = 1$ state of G symmetry was measured [28] and a value of $\pm(0.10 \pm 0.01)$ D was obtained. We have calculated this dipole by means of our different potentials, see Table 5. Notice that potential **III** gives good agreement: −0.13 D. The dipole surface used in this

Table 5
Energy splittings and dipoles for the lowest G states with $|\Omega| = 1$

	I	II	III	IV	Exp.
$E_1 - E_0$ (GHz)	255.7	226.4	186.1	168.5	118.1[a]
$E_2 - E_0$ (GHz)	582.0	969.5	483.9	740.8	486.4[a]
$E_3 - E_0$ (GHz)	977.8	1103.3	975.9	1159.8	865.1[a]
$\langle\mu\rangle_0$ (D)	0.31	0.057	−0.13	−0.046	0.10[b]
$\langle\mu\rangle_1$ (D)	−0.96	−0.44	−0.85	−0.50	–
$\langle\mu\rangle_2$ (D)	−0.29	−0.033	0.12	0.029	< 0.09[b]

[a] Ref. 25.
[b] Ref. 28. Experimentally the sign is undetermined.

calculation was the same as in Ref. 24 and consists of a permanent dipole and a dipole-induced dipole on either monomer. Also in Table 5 we compare the energy splittings of the lowest $G|\Omega| = 1$ states with those found by Loeser et al. Again potential **III** gives the best agreement. We present the splittings found by the use of potential **III** graphically in Fig. 9, together with the corresponding experimental values. The expectation value of the dipole in each state is given in this figure as well. Given the simplicity of all our model potentials, including potential **III**, the agreement between the computed and corresponding experimental numbers is surprisingly good.

4. Discussion and conclusions

First of all, let us mention that the four model potentials introduced in Section 2, which all have interchange barriers between 0 and 30 cm^{-1}, yield substantially better agreement with the microwave and far-infrared spectra than the potential that we used earlier [24], which has a barrier of $\approx 80\,cm^{-1}$. Potentials **I** and **III** which have barriers of about 30 cm^{-1} give good interchange tunneling splittings $E_{A_4} - E_{A_1}$, $E_{E_1} - E_{E_2}$, and $E'_G - E_G$ (see Tables 4 and 5). The splittings obtained from potentials **II** and **IV**, which have practically no barriers, are too high. The angles θ_A and θ_B that correspond to the nuclear quadrupole splittings are fairly close to the experimental values [17] for all the model potentials, much closer than the results in our earlier paper [24]. The best dipole moment, measured for the ground state of G symmetry just as the quadrupole splittings, is obtained from potential **I**. The other potential that yields realistic interchange tunneling splittings, potential **III**, gives a dipole moment which is just slightly too large. Remember that the dipole moment is 2.29 D in the nearly linear hydrogen-bonded structure that corresponds to the equilibrium structure of the potential in Ref. 24, while the average dipole in that paper is 1.60 D. Even for potential **I** with its good

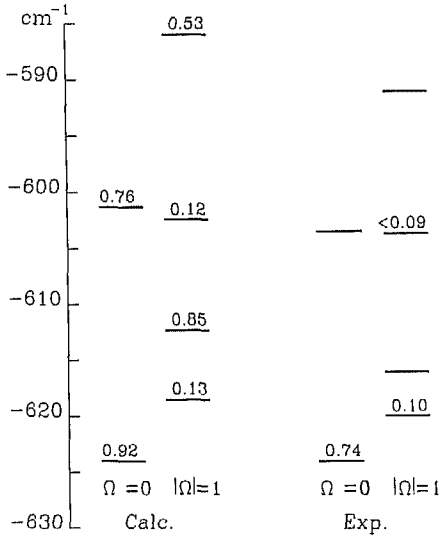

Fig. 9. Energy splittings and dipoles of the lowest G states. The computed results on the left-hand side are all obtained from potential **III**. The absolute values of the dipole expectation values, given at each level, are in debyes. The experimental values on the right-hand side are from Refs. 25 and 28. The experimental energy levels have been aligned to the computed energy zero.

average dipole moment of 0.69 D, the dipole that corresponds with the equilibrium geometry of the dimer is still 1.49 D. This is characteristic for the lack of rigidity of $(NH_3)_2$ along the interchange coordinate, as are the deviations between the average angles θ_A and θ_B obtained from the quadrupole splittings and the average angles that correspond with the dipole moment. Yet another sign of this non-rigidity is the recent [28] finding that the dipole moment of the lowest G state with $|\Omega| = 1 (\mu = 0.10\,D)$ is much smaller than the dipole ($\mu = 0.74\,D$) of the ground state with $\Omega = 0$. This finding is qualitatively reproduced by all the present model potentials; potential **III** gives the best quantitative agreement ($|\mu| = 0.13\,D$). Our calculations predict further that the first excited G state with $|\Omega| = 1$ has a much larger dipole moment, which does not differ much from the ground state $\Omega = 0$ value. It should be possible to check this prediction experimentally by the measurement of Stark splittings. Furthermore, we observe in Fig. 9 that the G levels with $|\Omega| = 1$ are now correctly positioned, relative to the G levels with $\Omega = 0$. In Ref. 24 we still found the lowest G level with $|\Omega| = 1$ to be $8\,cm^{-1}$ below the lowest level with $\Omega = 0$.

Regarding the level splittings $E_{E_1} - E_{E_3}$ and $E_{E_2} - E_{E_4}$ one can make the following observations. When looking at the quantum numbers k_A and k_B that characterize the basis functions of these symmetries (see Table 4 of Ref. 24), one observes that these splittings are related to the barriers in the rotations of the NH_3 monomers about their C_3 axes. Since $k_A, k_B = 1, -1$ (mod 3) for the states of E_1 and E_2 symmetry and $k_A, k_B = 1, 1$ (mod 3) for the states of E_3 and E_4 symmetry, the first states perform anti-geared rotations over ϕ_A and ϕ_B and the latter states correspond with geared rotations. Note that the orientations of the two C_3 axes of the NH_3 monomers themselves (the angles θ_A and θ_B) exhibit large oscillations, however. It is striking that the measured values [25] for these splittings are extremely small, given that these splittings are caused by the potential rather than by weak Coriolis interactions. Although our calculated values of 1 to $5\,cm^{-1}$ for these splittings are small too, they are still a few orders of magnitude larger than the measured splittings. The fact that these observed splittings are so minute should give us information about some characteristics of the intermolecular potentials. We are presently studying models with two coupled rotors in order to understand the data. The interpretation is not easy, however, since in reality, the different degrees of freedom in the $(NH_3)_2$ dimer are strongly coupled. Moreover, there are different extreme cases, either with free rotations or with rotations completely quenched, which lead to the limit of zero splittings.

All the model potentials of the present paper yield quite realistic values for the umbrella inversion splittings. Remember that this splitting in the free NH_3 monomer amounts to 23 GHz. In the last two lines of Table 4 we see that in the dimer this tunneling motion is about 10 times slower, which is correctly reflected by all the model potentials. Group theory shows (see Ref. 38) that the observed G state splittings correspond with the inversion of the para monomer. Our calculations tell us that in the ground state of G symmetry (with $\Omega = 0$) this is predominantly the proton donor, in the first excited G state with $\Omega = 0$ it is the proton acceptor. Although, of course, the difference between the acceptor and the donor vanishes for the cyclic structure, it is still (slightly) present even when the potential has a cyclic equilibrium geometry, due to the inequivalence of the ortho and para monomers in the G states. So, the experimentally observed inversion splittings imply that the inversion of the proton donor is less hindered than the inversion of the acceptor, a fact which is correctly reflected by all the calculated results. From the wavefunctions obtained in Ref. 24 we calculate inversions splittings of 1.67 GHz and 0.09 GHz, for the ground and first excited G state, respectively. Again, we find that the present potentials, which yield more nearly equivalent monomers, give far better results than the potential used in Ref. 24.

We have already considered the ϕ_A and ϕ_B

dependence of the intermolecular potential when we discussed the small splittings $E_{E_1} - E_{E_3}$ and $E_{E_2} - E_{E_4}$. We have to make another observation regarding this ϕ_A, ϕ_B dependence. It seems surprising that the potentials **I** and **II**, on the one hand, and the potentials **III** and **IV**, on the other, yield very similar results for the energy level splittings and the other observed properties, whereas they differ strongly in their ϕ_A, ϕ_B dependence. In particular, owing to the effects of the octupole moments in potentials **III** and **IV**, the equilibrium values of ϕ_A and ϕ_B are 60° and 0°, respectively, while for potentials **I** and **II** these values are 0° and 60° (see Table 3). It can be proved, however, that a transformation of the intermolecular potential that corresponds to a rotation of both ϕ_A and ϕ_B by 60° (mod 120°) leaves the eigenvalues of the rovibrational Hamiltonian invariant and conserves also the G_{36} symmetry. This is related with the fact that the NH_3 monomers are symmetric tops, with kinetic energy operators that are invariant with respect to any rotation over the angles $\phi_X (X = A \text{ or } B)$. The eigenstates do rotate with the potential over $\phi_A, \phi_B = 60°, 60°$, but the calculated dipole moment and quadrupole splittings which depend only on the θ_A and θ_B angles, are not affected. These quantities are affected, however, by the fact that potentials **I** and **II** and potentials **III** and **IV** have rather different barriers in the ϕ_A and ϕ_B rotations (see Table 3), due to the presence of the octupole interactions in the latter. We observe, in particular, that the higher C_3 rotation barriers enhance the different behavior of ortho and para monomers. This, in turn, influences the difference between the average values of θ_A and θ_B in the G states and, thereby, increases the average dipole moment (see Table 4).

In our final conclusion, we return to the question in the title of this paper: is $(NH_3)_2$ hydrogen bonded? We think that the intermolecular potential in this dimer must be close to our model potential **III**, because this potential yields VRT level splittings and properties which agree well with the spectroscopic data. In this potential, as well as in our other model potentials, the stabilization of this dimer is mostly of electrostatic origin. The purely electrostatic interactions favor a nearly linear hydrogen bond. Remember that the dipole and quadrupole moments already provide the angles θ_A and θ_B which are appropriate for a nearly linear hydrogen bond, but that one needs the non-axial octupole moments to bring the protons of the NH_3 proton donor to the direction of the lone pair of the acceptor NH_3. The electrostatic interactions lead to a rather deep valley, with a saddle point between the two equivalent nearly linear hydrogen-bonded structures. The barrier at this saddle point is low in comparison with the energy needed to climb the slopes of this valley. The electrostatic valley is so dominant that it stays when the exchange repulsion and dispersion interactions are added. The interchange barrier between the two equivalent minima is lowered especially by the exchange repulsion between the protons and the lone pairs. For potential **III**, which gives the best overall agreement with the experimental data, the remaining barrier is only $24\,cm^{-1}$. The fact that this barrier is so low (recall that the binding energy D_e is more than $1000\,cm^{-1}$) and that the electrostatic and the exchange repulsion contributions nearly cancel (so that the, smaller, induction and dispersion terms will be important too), makes it hard for ab initio calculations to give an accurate prediction of the barrier height. The result of this low barrier is that $(NH_3)_2$ becomes much less rigid than other hydrogen-bonded dimers, such as $(HF)_2$ and $(H_2O)_2$. Since the near linearity of $A–H\cdots B$ is the most characteristic feature of hydrogen bonding, we must conclude that $(NH_3)_2$ is not hydrogen bonded. Some of the features of hydrogen bonding persist, however. Although the average structure calculated from potential **III** is nearly cyclic, the equilibrium structure in this potential is still close to a linear hydrogen-bonded structure. This equilibrium structure, and also the height of the interchange barrier, agree quite well with the ab initio results of Hassett et al. [22]. Further, we observe that the attractive electrostatic interactions between the protons and the lone pairs of

the NH_3 monomers allow only a specific coupled internal rotation of both monomers, along the interchange path. So, the directionality that characterizes a hydrogen bond is not completely lost in $(NH_3)_2$.

5. Acknowledgements

We thank Rich Saykally and Jenny Loeser (Berkeley), Leo Meerts and Harold Linnartz (Nijmegen), Martina Havenith (Bonn) and Wolfgang Stahl (Kiel) for making available their experimental data before publication and for numerous stimulating discussions.

6. References

1 J.T. Brobjer and J.N. Murrell, Mol. Phys., 50 (1983) 885.
2 G.C. Hancock, D.G. Truhlar and C.E. Dykstra, J. Chem. Phys., 88 (1988) 1786.
3 M. Kofranek, H. Lischka and A. Karpfen, Chem. Phys., 121 (1988) 137.
4 P.R. Bunker, M. Kofranek, H. Lischka and A. Karpfen, J. Chem. Phys., 89 (1988) 3002.
5 P.R. Bunker, P. Jensen, A. Karpfen, M. Kofranek and H. Lischka, J. Chem. Phys., 92 (1990) 7432.
6 H. Kistenmacher, H. Popkie, E. Clementi and R.O. Watts, J. Chem. Phys., 60 (1974) 4455.
7 B. Jeziorski and M.C. van Hemert, Mol. Phys., 31 (1976) 713.
8 D.F. Coker and R.O. Watts, J. Phys. Chem., 91 (1987) 2513.
9 K. Szalewicz, S.J. Cole, W. Kołos and R.J. Bartlett, J. Chem. Phys., 89 (1988) 3662.
10 S. Rybak, B. Jeziorski and K. Szalewicz, J. Chem. Phys., 95 (1992) 6576.
11 B.J. Howard, Th.R. Dyke and W. Klemperer, J. Chem. Phys., 81 (1984) 5417.
12 H.S. Gutowsky, C. Chuang, J.D. Keen, T.D. Klots and T. Emilsson, J. Chem. Phys., 83 (1985) 2070.
13 A.S. Pine and B.J. Howard, J. Chem. Phys., 84 (1986) 590.
14 G.T. Fraser, Int. Rev. Phys. Chem., 10 (1991) 189, and references cited herein.
15 E. Zwart, J.J. ter Meulen and W.L. Meerts, J. Mol. Spectrosc., 147 (1991) 27.
16 N. Pugliano, J.D. Cruzan, J.G. Loeser and R.J. Saykally, J. Chem. Phys., 98 (1993) 6600.
17 D.D. Nelson, Jr., G.T. Fraser and W. Klemperer, J. Chem. Phys., 83 (1985) 6201.
18 K.P. Sagarik, R. Ahlrichs and S. Brode, Mol. Phys., 57 (1986) 1247.
19 S. Liu, C.E. Dykstra, K. Kolenbrander and J.M. Lisy, J. Chem. Phys., 85 (1986) 2077.
20 Z. Latajka and S. Scheiner, J. Chem. Phys., 84 (1986) 341.
21 M.J. Frisch, J.E. Del Bene, J.S. Binkley and H.F. Schaefer, J. Chem. Phys., 84 (1986) 2279.
22 D.M. Hassett, C.J. Marsden and B.J. Smith, Chem. Phys. Lett., 183 (1991) 449.
23 F.-M. Tao and W. Klemperer, J. Chem. Phys., 99 (1993) 5976.
24 J.W.I. van Bladel, A. van der Avoird, P.E.S. Wormer and R.J. Saykally, J. Chem. Phys., 97 (1992) 4750.
25 J.G. Loeser, C.A. Schmuttenmaer, R.C. Cohen, M.J. Elrod, D.W. Steyert, R.J. Saykally, R.E. Bumgarner and G.A. Blake, J. Chem. Phys., 97 (1992) 4727.
26 M. Havenith, R.C. Cohen, K.L. Busarow, D-H. Gwo, Y.T. Lee and R.J. Saykally, J. Chem. Phys., 94 (1991) 4776.
27 M. Havenith, H. Linnartz, E. Zwart, A. Kips, J.J. ter Meulen and W.L. Meerts, Chem. Phys. Lett., 193 (1992) 261.
28 H. Linnartz, A. Kips, W.L. Meerts and M. Havenith, J. Chem. Phys., 99 (1993) 2449.
29 C.E. Dykstra and L. Andrews, J. Chem. Phys., 92 (1990) 6043.
30 P.E.S. Wormer and H. Hettema, J. Chem. Phys., 97 (1992) 5592.
31 L. Pauling, The Nature of the Chemical Bond, 3rd Edn., Cornell University Press, Ithaca, NY, 1960.
32 D.M. Brink and G.R. Satchler, Angular Momentum, 2nd Edn., Oxford University Press, 1968.
33 G. Brocks, A. Van der Avoird, B.T. Sutcliffe and J. Tennyson, Mol. Phys., 50 (1983) 1025.
34 Handbook of Chemistry and Physics, CRC, Cleveland, 1974–1975.
35 J. Tennyson and B.T. Sutcliffe, J. Chem. Phys., 77 (1982) 4061; 79 (1983) 43.
36 J.W.I. van Bladel, A. van der Avoird and P.E.S. Wormer, J. Phys. Chem., 95 (1991) 5414.
37 D. Papoušek, J.M.R. Stone and V. Špirko, J. Mol. Spectrosc., 48 (1973) 17.
38 E.H.T. Olthof, A. van der Avoird and P.E.S. Wormer, in preparation.